1   Substantially positive contributions of new particle formation to Cloud Condensation

2   Nuclei under low supersaturation in China based on numerical model improvements

4   Chupeng Zhang[1#], Shangfei Hai[2,11#], Yang Gao[1*], Yuhang Wang[3*], Shaoqing Zhang[4,2],

5   Lifang Sheng[2], Bin Zhao[5], Shuxiao Wang[5], Jingkun Jiang[5], Xin Huang[6], Shen

6   Xiaojing[7], Sun Junying[7], Aura Lupascu[8] ,Manish Shrivastava[9], Jerome D. Fast[9],

7   Wenxuan Cheng[1], Xiuwen Guo[1], Ming Chu[1], Nan Ma[10], Juan Hong[10], Qiaoqiao

8   Wang[10], Xiaohong Yao[1] and Huiwang Gao[1]

10   [1]Frontiers Science Center for Deep Ocean Multispheres and Earth System, and Key Laboratory of

11   Marine Environmental Science and Ecology, Ministry of Education, Ocean University of China,

12   and Laoshan Laboratory, Qingdao, 266100, China

13   [2]College of Oceanic and Atmospheric Sciences, Ocean University of China, Qingdao, 266100,

14   China

15   [3]School of Earth and Atmospheric Sciences, Georgia Institute of Technology, Atlanta, GA, 30332,

16   USA

17   [4]Frontiers Science Center for Deep Ocean Multispheres and Earth System, and Key Laboratory of

18   Physical Oceanography, Ocean University of China, and Laoshan Laboratory, Qingdao, 266100,

19   China

20   [5]State Key Joint Laboratory of Environment Simulation and Pollution Control, School of

21   Environment, Tsinghua University, Beijing, 100084 China,and State Environmental Protection

22   Key Laboratory of Sources and Control of Air Pollution Complex, Beijing 100084, China

23   [6]School of Atmospheric Sciences, Nanjing University, Nanjing, 210023, China

24   [7]State Key Laboratory of Severe Weather & Key Laboratory of Atmospheric Chemistry of CMA,

25   Chinese Academy of Meteorological Sciences, Beijing, 100081, China

26   [8]Institute for Advanced Sustainability Studies, Potsdam D-14467, Germany

27   [9]Atmospheric Sciences and Global Change Division, Pacific Northwest National Laboratory,

28   Richland, WA, 99354, USA

29   [10]Institute for Environmental and Climate Research, Jinan University, Guangzhou, 510000, China

30   [11]CMA Earth System Modeling and Prediction Center, China Meteorological Administration,

31   Beijing 100081, China

32   [#]Authors contributed equally to this study.

33   [*]To whom correspondence to: yanggao@ouc.edu.cn, yuhang.wang@eas.gatech.edu

34

35

Abstract

New particle formation (NPF) and subsequent particle growth are important sources of condensation nuclei (CN) and cloud condensation nuclei (CCN). While many observations have shown positive contributions of NPF to CCN at low supersaturation, negative NPF contributions were often simulated in polluted environment. Using the observations in a typical coastal city of Qingdao, we thoroughly evaluate the simulated number concentrations of CN and CCN using a NPF-explicit parameterization embedded in WRF-Chem model. In terms of CN, the initial simulation shows large biases of particle number concentrations at 10–40 nm (CN_{10-40}) and 40–100 nm (CN_{40-100}). By adjusting the process of gas-particle partitioning, including mass accommodation coefficient of sulfuric acid, the phase changes of primary organic aerosol emissions and the condensational amount of nitric acid, the concomitant improvement of the particle growth process yields a substantial reduction of overestimates of CN_{10-40} and CN_{40-100}. Regarding CCN, SOA formed from the oxidation of semi-volatile and intermediate volatility organic vapors (SI-SOA) yield is an important contributor. In the original WRF-Chem model with 20 size bins setting, the yield of SI-SOA is too high without considering the differences in oxidation rates of the precursors. Lowering the SI-SOA yield results in much improved simulations of the observed CCN concentrations. On the basis of the bias-corrected model, we find substantial positive contributions of NPF to CCN at low supersaturation (~0.2%) in Qingdao and over the broad areas of China, primarily due to the competing effects of increasing particle hygroscopicity surpassing that of particle size decrease. This study highlights the potentially much larger NPF contributions to CCN on a regional and even global basis.

1. Introduction

New particle formation (NPF) is a process in which gaseous vapors nucleate and form critical molecular clusters, followed by subsequent growth to larger sizes through condensation and coagulation (Kulmala et al., 2004; Kulmala et al., 2013; Lee et al., 2019). Newly formed particles could effectively grow into the size of cloud condensation nuclei (CCN) under certain supersaturation (SS), which exerts an impact on the cloud microphysical process and global radiation balance (Merikanto et al., 2009; Gordon et al., 2017; Kerminen et al., 2018; Ren et al., 2021). In addition, the efficient nucleation and explosive growth of particles may contribute to the formation of haze (Guo et al., 2014), affecting air quality and human health (Yuan et al., 2015; Chu et al., 2019; Kulmala et al., 2021).

The overestimate of condensation nuclei (CN) in numerical models are commonly seen, despite the attempt to rectify the bias (Matsui et al., 2013; Arghavani et al., 2022). It is a common way to reduce the nucleation rate which may reduce the particle number concentration in proportion (Matsui et al., 2013). For instance, in the study of NPF in East Asia in the spring of 2009, even after lowering the nucleation rate in a regional model of WRF-Chem applied in their study, the reduced number concentration of particles at 10–130 nm remained to be overestimated (Matsui et al., 2013). Using the same regional model and a similar method to reduce the nucleation rate, Arghavani et al. (2022) found particle number concentration at 10–100 nm was still overestimated by nearly one order of magnitude, despite the effectiveness to reduce the overestimates for the smaller particles such as 2.5–10 nm. In addition to the rate of NPF, the growth process of particles also has a crucial effect on particle number concentration and size distribution. In this process, the condensation of some chemical species such as sulfuric acid, nitrate and organic gases on particles plays a major role in particle growth (Yao et al., 2018; Lee et al., 2019; Li et al., 2022), and the uncertainty of their condensation amount may lead to the bias of CN simulation.

In addition to CN, there are large discrepancies in the predicted CCN between the numerical models and observational results. Furthermore, as an important source of CCN (Merikanto et al., 2009), the contribution of nucleation to CCN quantified by

96   numerical models is also highly uncertain. For example, in terms of predicting CCN,

97   Fanourgakis et al. (2019) evaluated the CCN concentrations simulated by 16 global

98   aerosol–climate and chemistry transport models with observations at 9 sites in Europe

99   and Japan from 2011 to 2015, and found that all models underestimated CCN

100 concentrations with a mean normalized mean bias of -36% at low supersaturation

101 (SS=0.2%). WRF-Chem models also tend to underestimate the contribution of NPF

102 on CCN, especially at low supersaturation. The continuous observation of CCN

103 concentrations throughout the year (July 2008–June 2009) carried out in Hyytiälä,

104 Finland, showed that under low SS, nucleation enhanced the CCN by 106% and 110%

105 at SS=0.1% and 0.2% respectively (Sihto et al., 2011). Observations acquired in

106 Beijing from July 12 to September 25, 2008, also suggested that nucleation

107 significantly increases CCN at all supersaturations, even when supersaturation is low

108 (i.e., 0.07% and 0.26%). Thus, the occurrence of NPF enhanced CCN by a factor of

109 1.7 and 2.2, respectively (Yue et al., 2011).

110   However, previous numerical experiments behave oppositely. For instance,

111 Matsui et al. (2011) quantified the contribution of nucleation to CCN using WRF-

112 chem in Beijing in August and September 2006 and found reduced CCN under low SS,

113 e.g., when SS=0.02%, the concentration of CCN is reduced by up to ~50%. They

114 attributed this to the fact that the small particles produced by nucleation may inhibit

115 the growth of the preexisting particles (Matsui et al., 2011). Similarly, Dong et al.

116 (2019) conducted NPF simulations with the WRF-Chem for the summer of 2008

117 focusing on the Midwest of the United States, and found that the nucleation resulted

118 in decreased CCN at low supersaturation (SS=0.1%). Besides, a study carried out for

119 East Asia in 2009 also indicated that at low supersaturation (e.g. SS=0.1%),

120 nucleation has little impact on CCN (Matsui et al., 2013). The contrasting effects of

121 nucleation on CCN at low supersaturations in model and observations is not explained

122 in these previous studies.

123   At the stage of particle growth, secondary organic aerosol (SOA) formed by

124 atmospheric oxidation of organic vapors is a major contributor to particle growth to

125 CCN-related sizes (Liu and Matsui, 2022; Qiao et al., 2021). SOA formed by multi-

generational gas-phase oxidation of semi-volatile and intermediate volatility organic compounds (S/IVOC) is called SI-SOA (Jimenez et al., 2009; Zhang et al., 2007). Zhao et al. (2016) made a comprehensive assessment of the roles of various SOA precursors in SOA formation in real atmosphere in China in 2010, and the results demonstrated that evaporated POA and IVOC (i.e. S/IVOC) made a significant contribution to SOA, contributing up to 82% to the average SOA concentration in eastern China. However, the effect of SI-SOA on CCN has not been fully studied.

In this paper, WRF-Chem was applied to simulate the effect of the NPF on CCN in Qingdao in February 2017. The simulated results from the WRF-Chem model are firstly compared with observations in Qingdao, exhibiting large biases in CN. This is followed by an improvement through a few processes. At the end, the impact of SI-SOA yield and nucleation on CCN is investigated.

2. Data and methods

2.1 Observations

The measurements used in this study were carried out over the sampling site from February 5 to 24, 2017 at the campus of Ocean University of China (36°09′37″N, 120°29′44″E) in Qingdao, which is surrounded by residential buildings and is situated about 10 km away from the city center. A fast mobility particle sizer (FMPS, TSI Model 3091) was applied to measure the aerosol particle size distribution for the size range of 5.6 nm to 560 nm (Liu et al., 2014b). The bulk CCN concentration is measured by a cloud condensation nuclei counter at three different supersaturations (0.2%, 0.4% and 0.6%) and each supersaturation lasts for 20 minutes. More information about the CCN measurement can be found in Li et al. (2015). The urban site in Beijing is located on the roof of the building of the Chinese Academy of Meteorological Sciences (CAMS, 39°95′N, 116°33′E) in the campus of the China Meteorological Administration, close to the main road with heavy traffic. The rural site is Gucheng (GC, 39°08′N, 115°40′E), located in Hebei Province, surrounded by farmland, and is a representative station of the severity of air pollution in Beijing Tianjin Hebei region. The particle number size distribution of these two sites in the range of 4–850 nm is measured by a Tandem Scanning Mobility Particle Sizer

156 (TSMPS), and more information about the instruments can be found in Shen et al.
157 (2018).

158 **2.2 Model configurations**

159   WRF-Chem version 3.9 is used to simulate NPF events, with the main physical

160 and chemical parameterization settings summarized in Table 1. The spatial resolution

161 is 36 km by 36 km with 35 vertical layers and a model top at 50 hPa. The regional

162 model simulations at a higher spatial resolution may be desirable in future when urban

163 pollution is focused. A continuous run from February 1 to 25, 2017, was conducted,

164 with the first five-day results as the spin-up and discarded in the analysis.

165 Table 1 WRF-Chem model configurations used in this work

	Model configuration
Microphysics	Morrison 2-moment microphysics scheme (Morrison et al., 2009)
Planetary Boundary Layer (PBL)	YSU boundary layer scheme (Hong et al., 2006)
Longwave and Shortwave Radiation	RRTMG longwave and shortwave radiation (Iacono et al., 2008)
Land model	Unified Noah Land Surface scheme (Chen and Dudhia, 2000; Tewari et al., 2016)
Cumulus	Grell-3D cumulus parameterization scheme (Grell, 1993)
Aerosol module	MOSAIC module (Zaveri et al., 2008; Matsui et al., 2011)
Gas-phase Chemistry	SAPRC-99 gas-phase chemistry scheme (Carter, 2000)

166

167   The meteorological initial and boundary conditions are driven by Climate

168 Forecast System model version 2 (CFSv2; (Saha et al., 2014)) reanalysis developed

169 by National Centre for Environmental Prediction (NCEP). The initial and boundary

170 chemical conditions of WRF-Chem are provided by Community Atmosphere Model

171 with Chemistry (CAM-Chem; (Buchholz et al., 2019)). Anthropogenic emissions for

172 the year of 2017 are obtained from the Multiresolution Emission Inventory for China

173 (MEIC, http://www.meicmodel.org/) emission dataset (Li et al., 2017; Zheng et al.,
174 2018).

175   The Model for Simulating Aerosol Interactions and Chemistry (MOSAIC) was
176 used to delineate dynamic gas-particle mass transfer to represent the condensation
177 growth of aerosol (Zaveri et al., 2008). The gas-particle partitioning of gas species on
178 particles is regulated by the mass transfer rate, which is related to mass
179 accommodation coefficient (α), a parameter involved in the model representing the
180 probability of gas molecules entering the bulk liquid phase (Pöschl et al., 1998). The
181 original setting of α for all condensing species for all size bins a in MOSAIC is 0.1
182 (Zaveri et al., 2008). In the default release of WRF-Chem, MOSAIC was
183 implemented in the sectional framework with aerosol size distributions divided into 4
184 or 8 size bins spanning 39 nm to 10 μm in diameter. To explicitly express the
185 nucleation and the growth of newly formed particles, the aerosol size range in the
186 MOSAIC module was extended from 1 nm to 10 μm, with the number of aerosol size
187 bins increased to 20 (Matsui et al., 2011; Matsui et al., 2013; Lupascu et al., 2015; Lai
188 et al., 2022). The calculation method of CCN concentration in the WRF-chem model
189 is referred to the study of Matsui et al. (2011). Based on Köhler theory, CCN
190 concentrations under the three given supersaturations of 0.2%, 0.4% and 0.6% were
191 calculated. The critical supersaturation (S_c) of each size bin in the WRF-chem model
192 was calculated by the following formula:

$$S_c = \sqrt{\frac{4 \times a^3}{27 \times r^3 \times \kappa}} \#(1)$$

$$a = \frac{2 \times \sigma}{R_v \times T \times \rho_\omega} \#(2)$$

193 Where α (m) is the coefficient of the Kelvin effect, κ is the volume−averaged
194 hygroscopicity, calculated using these values in Table 1, r (m) is the dry diameter, σ is
195 droplet surface tension over water (0.076 N m^{-1}), R_v is the gas constant for water
196 vapor (461.6 J K^{-1}kg^{-1}), T (K) is the air temperature, and ρ_ω is the density of water
197 (1000 kg m^{-3}).

              Table 2 Hygroscopicity Parameters (κ) in the WRF-Chem Model

Species	Hygroscopicity (κ)
Sulfate	0.5
Ammonium	0.5
Nitrate	0.5
Black carbon	10^{-6}
Primary organic aerosol	0.14
Other inorganics	0.14
Sodium	1.16
Chloride	1.16

199

200   The chemical aging process of organic aerosols (OA) is modeled by the volatility

201   basis set (VBS) approach, which was widely used in air quality models to represent

202   complex mixtures of thousands of organic species (Donahue et al., 2006; Shrivastava

203   et al., 2011; Chrit et al., 2018). The VBS method classifies compounds according to

204   the effective saturation concentration (c^*), which represents the proportion of the

205   component in the gas phase to the particle phase (Donahue et al., 2006), and species

206   with higher c^* values are more volatile. The oxidation of highly volatile precursors to

207   form relatively low volatile components represents the aging process of OA. OA

208   consists of directly emitted primary organic aerosols and photochemically produced

209   secondary organic aerosols (SOA) (Shrivastava et al., 2011). In this study, the

210   simplified 2-species VBS mechanism was applied to the simulation of SOA, during

211   which primary organic aerosol was represented by two species based on volatility

212   with effective saturation concentration c^* values (at 298 K and 1 atm) of 10^{-2} and 10^5

213   μg m^{-3} (Shrivastava et al., 2011). Primary organic aerosols with c^* of 10^5 μg m^{-3}

214   refers to S/IVOC, which is in the gas phase under most atmospheric conditions due to

215   its high volatility, while for those primary organic matters with c^* of 10^{-2} μg m^{-3}, is

216   treated as gas phase as well in the original model. The SOA formed by photochemical

217   oxidation of S/IVOC precursors is called SI-SOA and the SOA formed by oxidation

218   of VOC precursors is named V-SOA. In the simplified 2-species VBS mechanism, SI-

SOA ($c*$ of 10^{-2}μg m^{-3}) is formed by the oxidation reaction of S/IVOC precursors ($c*$ of 10^5μg m^{-3}) and OH with an oxidation rate constant of 4×10^{-11} cm^3 molec^{-1} s^{-1}. The equations for controlling the oxidation of S/IVOC precursors are as follows:

$$POA(g)_{e,c} + OH \rightarrow SI - SOA(g)_{e,c} + 0.15SI - SOA(g)_{e,o} \#(3)$$

$$POA(g)_{e,o} + OH \rightarrow SI - SOA(g)_{e,o} + OH \#(4)$$
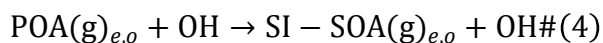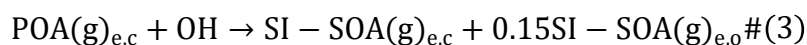
where POA(g) denotes primary organic aerosols with $c*$ of 10^5 μg m^{-3}, which reacts with OH to form SI-SOA(g) with $c*$ of 10^{-2} μg m^{-3}. Subscripts c and o represent the non-oxygen and oxygen parts respectively of given species and e is either the biomass or anthropogenic emission sector. In addition, SVOC and IVOC emissions corresponding to both anthropogenic and biomass burning emissions are derived based on constant emission ratio of S/IVOC to POA (Shrivastava et al., 2011). A detailed description of 2-species VBS mechanism can be found in Shrivastava et al. (2011).

2.3 Model sensitivity formulations

Three sets of sensitivity tests are designed and listed in Table3. The purposes of the three sets of experiments are as follows: (1) Adjust the condensation growth process of ultrafine particles in WRF-Chem model (Base, MAC, POA, NOCD, RACD, with details in Table 3).; (2) Explore the effect of SI-SOA yield on CCN (Low-Yield and High_Yield); (3) Study the effect of nucleation process on CCN under the change of SI-SOA yield (Low-Yield and High_Yield and their corresponding cases without nucleation parameterization, i.e., Low_nucoff and High_nucoff). Each scenario will be explained in conjunctions with the results.

 Table 3 The sensitivity tests involved in this study

Purposes	Simulation scenarios	Description
Adjust the condensation growth process of ultrafine particles	Base	Simulation with the default setting with nucleation coefficient set as 2×10^{-6} s^{-1}, the same as Lai et al. (2022)
	Mass accommodation coefficient (MAC)	It is the same as Base except that the mass adjustment coefficient (α) of gaseous sulfuric acid is adjusted from 0.1 to 0.65.
	POA emission phase (PEP)	It is the same as MAC except that the phase of POA is changed from gas phase to particle phase.
	No condensation (NOCD)	It is the same as PEP except that no NH_4NO_3 condenses on particles below 40 nm.
	Ratio method for condensation (RACD)	It is the same as PEP except that the condensation of NH_4NO_3 on particles below 40 nm is reduced according to the ratio of acid particles to total particles reported in Wang et al. (2014).
Explore the effect of SI-SOA yield on CCN (Explore the effect of nucleation process on CCN under the change of SI-SOA yield)	High_Yield	Simulation with high oxidation rate of SI-SOA formation with reaction rate constant of 5×10^{-11} cm^3 molec^{-1} s^{-1}
	Low-Yield	Simulation with low oxidation rate of SI-SOA formation with reaction rate constant of 2×10^{-11} cm^3 molec^{-1} s^{-1}

Explore the effect of nucleation process on CCN under the change of SI-SOA yield	High_NUCOFF	Simulations without nucleation parameterizations based on High_Yield
	Low_ NUCOFF	Simulations without nucleation parameterizations based on Low-Yield

251

3. Results

3.1 Observational analysis

Based on the criteria (Dal Maso et al., 2005; Kulmala et al., 2012), NPF is defined as an event with the emergence of a nucleation mode with particle diameters smaller than 25 nm, lasting for 2 hours or more, followed in general by a continuous particle growth. Six NPF events were identified in February 2017 in Qingdao, on the days of 6, 9, 10, 17, 20 and 23 (Fig. 1a), yielding a frequency of ~30% and displaying a typical banana-shaped growth of particles in the particle number size distribution. Compared to a few other studies on NPF frequency in Qingdao, the results in this study are to a large extent consistent with that in the fall of 2012–2013 (30%; (Zhu et al., 2019)), slightly higher than that in summer 2016 (22%; (Zhu et al., 2019)) and lower than that in spring of 2010 (41%; (Liu et al., 2014c). The higher frequency in spring in Qingdao is consistent with the observational results at different stations in the Northern Hemisphere in Nieminen et al. (2018).
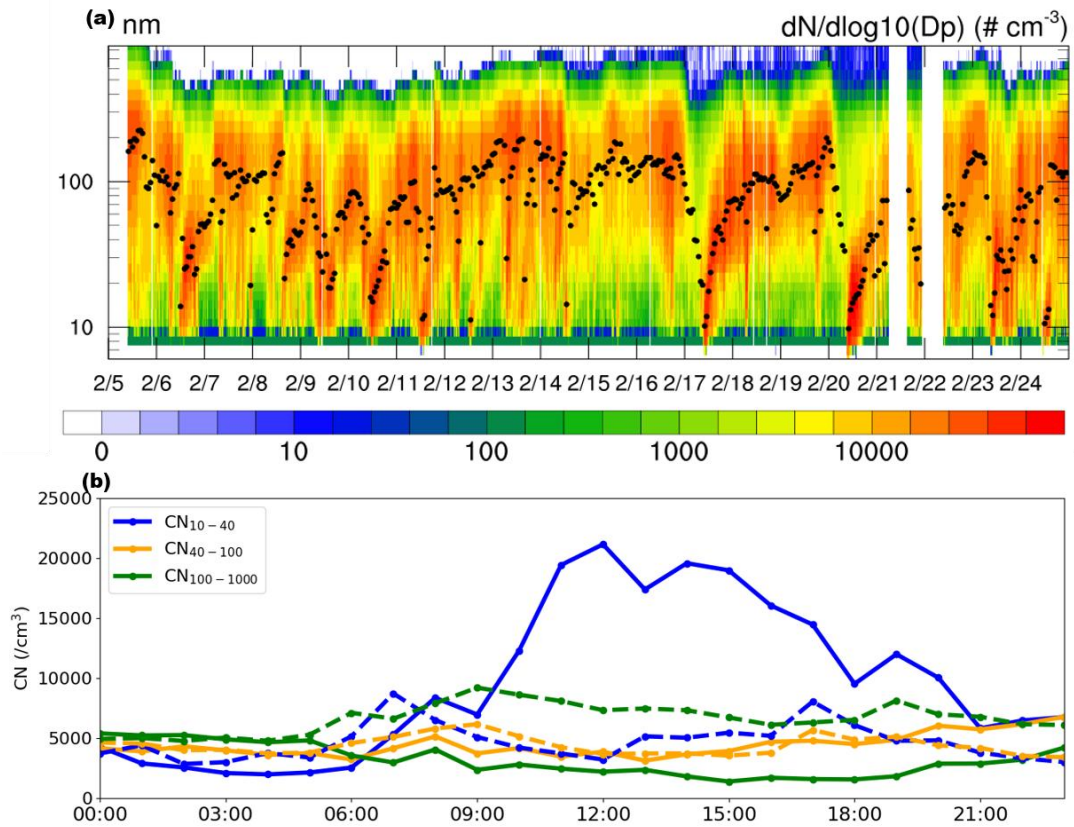
Fig. 1. Distribution of particle number concentration. (a) Temporal evolution of particle size distributions (colored shading) and geometric median diameter (GMD; dots in black) in Qingdao on February 5-24, 2017. (b) The mean diurnal variation of CN_{10-40} (blue), CN_{40-100} (orange) and $CN_{100-1000}$ (green) composited during the NPF (solid lines) and non-NPF (dashed lines) days on February 5-24, 2017. All times are local times (LT)

During the six NPF events identified in February in Qingdao, the mean diurnal cycle of CN_{10-40} (10–40 nm) particles exhibits triple peaks (solid blue in Fig. 1b), in the morning (8:00 LT), noon (12:00–14:00 LT) and evening (19:00 LT), respectively. A comparable three-peak feature was also observed in earlier years during 2016-2018 in Qingdao (Zhu et al., 2021). The morning and evening peaks of CN_{10-40}, with values of ~5300 cm^{-3} and ~12000 cm^{-3}, respectively, are likely caused by the primary emissions from traffic and cooking activities (Wu et al., 2021a; Wang et al., 2022; Cai et al., 2020). The occurrence of NPF starts approximately at 9:00 am LT, accompanied by a substantial increase in CN_{10-40} compared with non-NPF days (solid vs. dashed

lines, in blue), yielding a peak around noon (20000 cm^{-3} during 12:00–14:00 LT). In addition, larger particles (e.g., CN$_{40-100}$ and CN$_{100-1000}$) displayed a slow or no increase in the afternoon.

3.2 Model improvement in particle number concentration simulations

Particle number concentrations, primarily in two ranges of 10–40 nm and 40–100 nm, are commonly simulated with large biases. In the smaller size range (10–40 nm), the particle number concentration is associated with NPF and particle growth. During NPF, despite differences among the formation mechanisms, H$_2$SO$_4$ is considered the common species (Yu, 2005; Lovejoy et al., 2004), which often suffer large biases (Cai et al., 2016; Matsui et al., 2011). In the size range of 40–100 nm, the particle number concentration is primarily affected by the condensation growth of particles below 40 nm, which is closely related to chemical components such as SOA and nitrate. Prior to the evaluation of particle number concentration, we first evaluate the compositions of PM$_{2.5}$ and criteria air pollutants including PM$_{2.5}$, PM$_{10}$, O$_3$, SO$_2$, CO, and NO$_2$, showing relatively low biases compared to observations (section S1 and Fig. S1 and Fig. S2 of the supporting information).

3.2.1 Bias correction of particle number concentration at 10–40 nm

In this study, as shown in Fig. 2, comparisons of CN$_{10-40}$ between simulations (red line in Fig. 2a) and observations (black line in Fig. 2a) results of the six NPF events mentioned in the previous section in Qingdao in February 2017 indicate that model overestimates CN$_{10-40}$ with mean fractional bias of 48%. As one of the major processes affecting the particle number concentration of 10–40 nm, nucleation is governed by the particle nucleation rate of 1 nm particles (cm^{-3} s^{-1}), which is closely associated with the concentration of H$_2$SO$_4$. For instance, in a commonly applied activation mechanism, the nucleation rate calculated by $J^* = K_{ACT} \times [H_2SO_4]$. Note that K$_{ACT}$ is the nucleation coefficient considering the physical properties and chemical species of nucleation process under different environments, indicating that a lumped chemical species are included in the scheme reflected primarily in the

nucleation coefficient k, set as 2×10^{-6} s^{-1} based on previous studies (Sihto et al., 2006; Riipinen et al., 2007). Dong et al. (2019) simulated NPF occurring in the summer of 2008 in the United States using the NPF-explicit WRF-Chem based on the activation mechanism, which overestimated the particle number concentration at 10–63 nm by nearly doubled, even when the K_{ACT} decreased by one order of magnitude (set at a very low value of 10^{-7} s^{-1}). Therefore, it is likely that the overestimation of particle number concentration in the smaller particle size segment is probably due to the bias of simulated sulfuric acid.
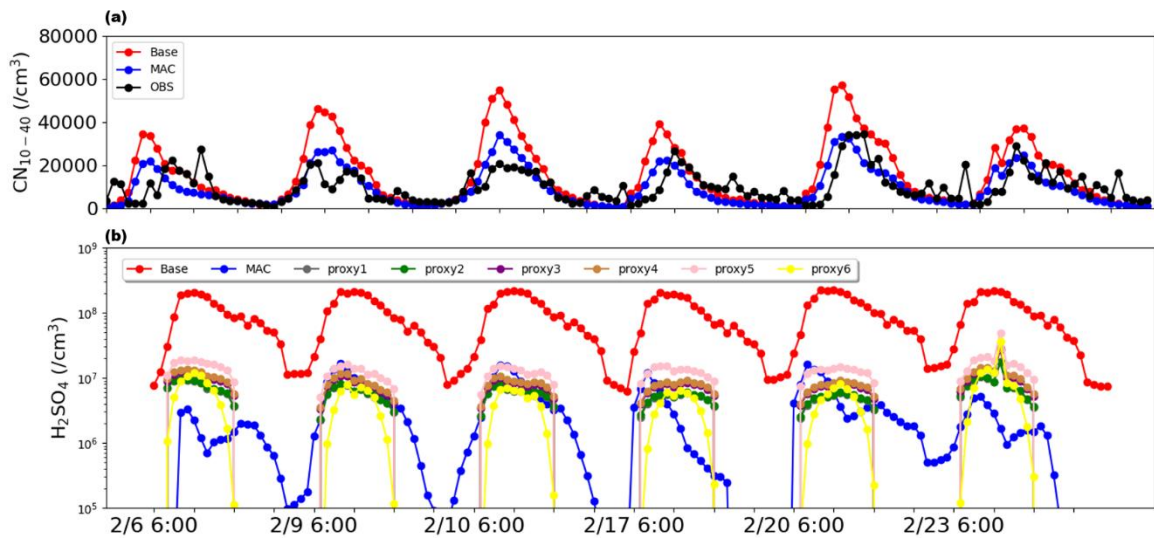
Fig. 2. Time series of (a) CN$_{10–40}$ on NPF days, where red and blue represent Base and MAC simulation results respectively, and black represents observation results, and (b) sulfuric acid gas concentration obtained by simulation and by proxies (dark grey: Eq. 5; green: Eq. 6; purple: Eq. 7; brown: Eq. 8; pink: Eq. 9; yellow: Eq. 10). All times are in local times.

Measurement of sulfuric acid gases in the lower troposphere is challenging due to the generally low ambient concentration of sulfuric acid (10^6–10^7 molecule cm^{-3}). Different methods have been proposed to estimate ambient sulfuric acid concentrations based on observations such as SO$_2$ (Petäjä et al., 2009; Lu et al., 2019; Mikkonen et al., 2011). For instance, Petäjä et al. (2009) proposed a linear method to approximate observed H$_2$SO$_4$ concentration in Hyytiala, southern Finland. Moreover, a recent study by Lu et al. (2019) proposed a nonlinear method to construct a number

335 of proxies for gaseous sulfuric acid concentration (Eq. 5–9), indicating that compared

336 to the linear method in Petäjä et al. (2009), the nonlinear relationship can provide

337 more accurate H_2SO_4 concentration in Beijing during February–March 2018 period.

338 In addition, we also used another sulfuric acid nonlinear proxy (Eq. 10) based on

339 long-term observations in Germany, Finland, the United States, etc. (Mikkonen et al.,

340 2011). In this study, we adopt the above six nonlinear proxy methods (referred as

341 proxy5 to proxy10) to estimate H_2SO_4 in Qingdao.

$$[H_2SO_4] = 515.74 \times [SO_2]^{0.38} \times \text{Radiation}^{0.14} \times CS^{0.03} \#(5)$$

$$[H_2SO_4] = 280.05 \cdot \text{Radiation}^{0.14} [SO_2]^{0.40} \#(6)$$

$$[H_2SO_4] = 9.95 \times [SO_2]^{0.39} \times \text{Radiation}^{0.13} \times CS^{-0.01} \times [O_3]^{0.14} \#(7)$$

$$[H_2SO_4] = 14.38 \times [SO_2]^{0.38} \times \text{Radiation}^{0.13} \times [O_3]^{0.14} \#(8)$$

$$[H_2SO_4] = 0.0013 \times [SO_2]^{0.38} \times \text{Radiation}^{0.13} \times CS^{-0.17} \times ([O_3]^{0.14} + [NO_x]^{0.41}) \#(9)$$

$$[H_2SO_4] = 8.21 \times 10^{-3} \times [SO_2]^{0.62} \times \text{Radiation} \times (CS \times RH)^{-0.13} \#(10)$$

342 where $[SO_2]$, $[O_3]$ and $[NO_x]$ (molecule cm^{-3}) represents concentration of

343 observed SO_2, O_3 and NO_x, respectively. "Radiation" (W m^{-2}) is global radiation. RH

344 (%) is the relative humidity, and CS (s^{-1}) is the condensation sink, which is calculated

345 based on observed particle distribution.

346 The simulated H_2SO_4 concentration from the Base simulation (dots in Fig. 2b) is

347 compared with observations obtained by proxies (see Fig. 2b), indicating that Base

348 simulations apparently overestimate by one order of magnitude compared to the

349 H_2SO_4 estimated by proxies. The overestimation has been frequently reported

350 previously, i.e., over Beijing (Matsui et al., 2011), which ascribes the bias to the

351 overestimation of the SO_2 concentration. In a more recent study, the sensitivity of

352 H_2SO_4 to SO_2 is tested, and the result shows that even when SO_2 is reduced to an

353 unrealistically low level, the simulated H_2SO_4 is still more than one order of

354 magnitude higher than the observed value (Lai et al., 2022), suggesting that the SO_2

355 concentration cannot fully explain the overestimates.

356 In addition to the precursor of H_2SO_4, the mass accommodation coefficient (α),

357 representing the probability of impaction of a gaseous molecule on a liquid surface

358   and entering the bulk liquid phase, is another important factor affecting the

359   concentration of sulfuric acid gas. In the public release of WRF-Chem, mass

360   accommodation coefficient is typically set to a low value of 0.1 for all gas species

361   under different volatility during the condensation process, including H_2SO_4

362   (Davidovits et al., 2004; Zaveri et al., 2008). Recent studies indicate that the low mass

363   accommodation coefficient value may not be applicable to the low volatile gases,

364   which tend to have a mean mass accommodation coefficient value of 0.7 and close to

365   the unity (Krechmer et al., 2017). In fact, an earlier study has indicated based on

366   experimental determination, the mass accommodation coefficient of H_2SO_4 vapor in

367   sulfuric acid aqueous solution was measured, and the best fit value was 0.65 (Pöschl

368   et al., 1998). Accordingly, a sensitivity simulation was conducted by adjusting the

369   mass accommodation coefficient of H_2SO_4 from 0.1 to 0.65, referred to as MAC.

370   This simulation brought the H_2SO_4 concentration (see Fig. 2b) much closer to the

371   calculated results from proxies, and the corresponding biases reduced by

372   approximately an order of magnitude. Notably, the MAC simulation decreases the

373   overestimate of sulfuric acid gas concentration, resulting in a lower particle formation

374   rate. The MAC simulation also significantly reduces overestimate of CN_{10-40} (Fig. 2a),

375   and mean fractional bias compared to observations decreases from 48% to 1%.

376

377   **3.2.2 Improvement of particle number concentration simulations at 40–100 nm**

378   The number concentration of particles in the 40–100 nm range is mainly affected

379   by the coagulation and condensation processes. While the coagulation process tends

380   to largely affect ultrafine particles below 10 nm than those with larger sizes (Wu et al.,

381   2011), the condensation growth of particles during gas-particle partitioning at sizes of

382   10–40 nm, to a large extent, governs the variations in number concentration of 40–

383   100 nm particles. The condensation process is primarily controlled by gas-particle

384   partitioning of chemical species, which may change the chemical composition of

385   particles, such as organic compounds and inorganics including sulfate, nitrate and

386   ammonium.

387   Among the species contributing to the condensation growth of particles at 10–40

nm, the organic compounds with $c*$ of 10^{-2} µg m^{-3} play the dominant role (Pierce et al., 2011). In the current model setting, the low volatile organic matter of 10^{-2} µg m^{-3} comes from two gas-phase sources, including the direct emission of primary organic aerosol (POA) and SOA formed from S/IVOC (SI-SOA), conducive to condensation on particles. While the condensation of gaseous SOA is in general reasonable, the gas phase emissions of POA may be problematic. For instance, previous studies suggested that POA is in gas phase close to the emissions source. However, with rapid dilution and cooling in the atmosphere away from the source, most POA condenses to particle-phase (Roldin et al., 2011b; Roldin et al., 2011a; Shrivastava et al., 2008). Therefore, away from the emissions source POA, being in the particle phase, will not be involved in the growth of newly formed particles. Therefore, POA may not contribute to particle growth away from the emission sources, which caused different size distributions of POA compared to when it was emitted in the gas-phase (Fig. S3a vs. Fig. S3b). Emitting low volatility POA in the particle phase eliminates the unreasonable quasi-banana shape pattern exhibiting concomitant growth of newly formed particles with increasing mass concentration of POA.

The composition analysis (Fig. S3c) in the 10–40 nm particles mass from the model results indicates that organic compounds mentioned above only account for 21% of total mass (sulfates, nitrates, ammonium salts and organics) in this size range and the dominant species is nitrate which accounts for 51% of total mass, exhibiting inconsistencies with the previous studies which in general indicates a much smaller contribution of nitrate. For instance, Liu et al. (2014a) suggested that over North China Plain in summer 2009, organic matter accounted for 77% of particles around 30 nm, while the sum of SO_4^{2-}, NO_3^- and NH_4^+ only accounted for 18%. Another study showed that nitrate accounted for 7–8% at urban sites and 17% at rural sites for particles mass in 7–30 nm in the United States in 2007 (Bzdek et al., 2012). Therefore, the potentially too high modeled nitrate fraction in 10–40 nm in this study is tightly associated with the condensation process, with the specific reasons explained below.

The condensation of nitric acid on particles is highly constrained by the particle acidity. The acidity in smaller particles (i.e., 10–40 nm) tends to be higher than that in

418   large particles, primarily due to the larger condensation of H_2SO_4 (Lu et al., 2022),

419   and particles with sizes greater than 40 nm have a much weaker acidity or are nearly

420   neutral. For example, observed evidence has shown that acidic ultrafine particles

421   account for a large proportion of ultrafine particles from 22 December 2010 to 15

422   January 2011 in Hong Kong, e.g., 65% for particles within 5.5–30 nm (Wang et al.,

423   2014).

424   In the model, a particle is determined to be in solid phase when the ambient

425   relative humidity is lower than the mutual deliquescence relative humidity of the

426   particles (Zaveri et al., 2005; Zaveri et al., 2008), which is in general suitable for

427   particles dominated by inorganics. In the study area, the results indicate that at most

428   conditions relative humidity are relatively low and the particles are in solid phase, in

429   which the condensation process is not affected by particle acidity and the

430   condensation of nitric acid on particles is directly calculated based on the gas-particle

431   equilibrium concentration (Zaveri et al., 2008). However, for particles below 40 nm,

432   the main compositions are likely to be organic matter (Zhu et al., 2014; Ehn et al.,

433   2014), which tends to be in liquid phase (Virtanen et al., 2011; Cheng et al., 2015),

434   under which the condensation of nitric acid is strongly constrained by acidity.

435   Therefore, the phase misrepresentation ignores the weakening effect of acidity on

436   nitric acid condensation, resulting in too high nitrate therein.

437   To overcome this issue, we propose a ratio method for condensation (RACD) to

438   partition the condensation of nitric acid on particles under 40 nm, by applying a ratio

439   of the number concentration of non-acidic particles to ultrafine particles. The method

440   is based on two assumptions, including: 1) little condensation of nitric acid on

441   particles with strong acidity (Lu et al., 2022); 2) the condensation of nitric acid on

442   particles is proportional to the ratio of the number concentration of non-acidic

443   ultrafine particles to the total particles, despite the existence of uncertainties. Fig. S4

444   depicts the average particle number concentration and acid particle in the 1 to 40 nm

445   range, calculated based on Wang et al. (2014). The ratio of non-acidic particles is 8%

446   for particles below 10 nm, 18% for particles at 10–15.8 nm, 30% for particles at 15.8–

447   25.1nm, and 55% for particles at 25.1–39.8 nm (Fig. S4). Note that the ratio is based

448 on measurements acquired at a single site in Hong Kong, therefore more

449 observational studies are needed to warrant the robustness of the method.

450 Alternatively, the condensation of nitric acid on particles in bins from 1nm to 40 nm is

451 completely suppressed, referred to as NOCD.

452   The simulation results based on the two methods (RACD and NOCD) are shown

453 in Fig. 3. Compared to MAC, RACD simulations reduce previously noted

454 overestimation of particle number concentration in the 40–100 nm size range (Fig. 3b),

455 with the mean fractional bias decreases from 83% to 63%. In addition to the amount

456 of nitrate condensation during particle growth mentioned above, the overestimation of

457 particle number concentrations in the 40–100 nm range may be attributed to

458 nucleation process. More specifically, in the H_2SO_4-H_2O binary nucleation

459 mechanism used in this study, when the concentration of sulfuric acid gas is reduced

460 (Section 3.2.1), the resulting decrease in nucleation rate leads to a slight decrease in

461 particle number concentration at 40–100 nm relative to Base (mean fractional bias

462 from 98% to 83%). Apart from that, it may also be related to the choice of nucleation

463 parameterization scheme. For example, using a global chemical transport model

464 GEOS-Chem with a nucleation mechanism in which formation rate is a function of

465 the concentrations of sulfuric acid and low-volatility organics, Yu et al. (2015)

466 overestimated the concentration of particles in the 10–100 nm range by 161% at nine

467 sites in the summer in North America. A possible explanation for this overestimation

468 was given by the uncertainty of the predicted concentration of organic compounds

469 involved in organics-mediated nucleation parameterization. After they switched to

470 another scheme of the ion-mediated nucleation mechanism without organic matter, the

471 number becomes 27% lower than the observations (Yu et al., 2015). The test based on

472 different schemes is beyond the scope of the study, which is therefore not investigated.

473   Moreover, the overestimation of particles over 100 nm ($CN_{100–1000}$; Fig. 3c), which

474 have a strong influence on CCN, also decrease in the RACD simulation. Thus, the

475 mean fractional bias decreases from 25% (MAC) to 1%. Note that the slight increase

476 of $CN_{10–40}$ through the application of RACD, can be linked to the decrease of nitrate

477 condensation, and leads to weakened particle growth and enhanced particle number

478 concentration at 10–40 nm (Fig. 3a). The alternative method by completely removing

479 the nitrate condensation (NOCD) yields even better performance in particle number

480 concentration of 40–100 nm (mean fractional bias of 34%), indicating the feasibility

481 by reducing the nitrate condensation. The proportion of nitrate simulated by RACD is

482 23%, closer to values reported in past observations (Bzdek et al., 2011; Bzdek et al.,

483 2012), while the nitrate (1%) in the scenario of NOCD seems to be too low.

484 Considering the limited observational information obtained based on previous studies,

485 RACD is applied in this study.

486 In addition to Qingdao, we evaluate the model performance over a few other sites,

487 including one site over urban Beijing and the other one over the rural area of Gucheng,

488 yielding consistent improvements in model simulations (Section S2; Fig. S6-S8).

489 Moreover, we select another empirical scheme, e.g., kinetics, and one classical

490 nucleation scheme, indicating the empirical scheme of activation scheme is in general

491 a good option in this study (Section S2; Fig. S9-S11; Table S1-3).

492
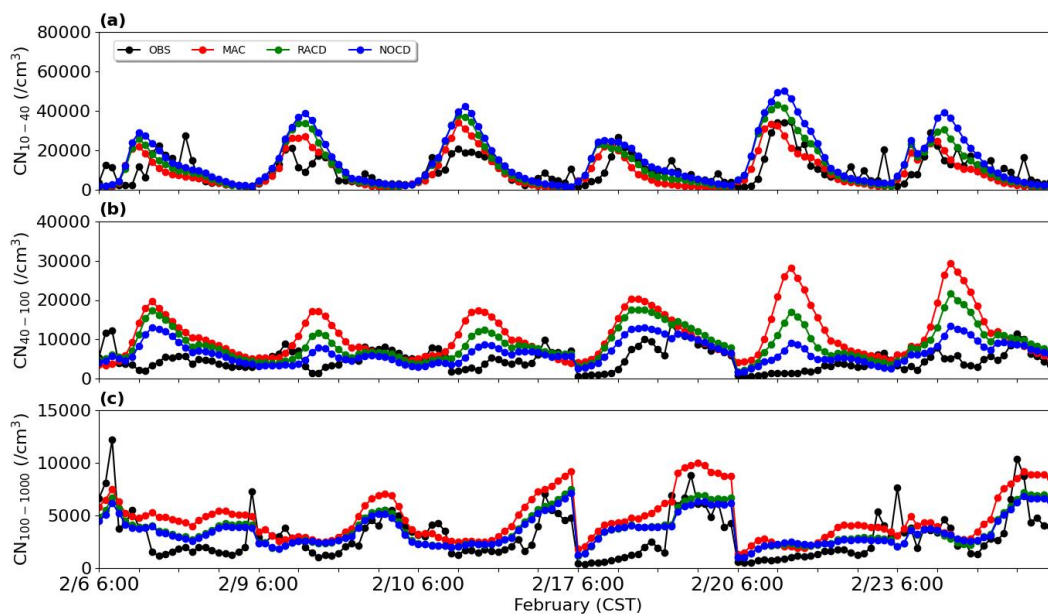
493 Fig. 3. The time series of (a) $CN_{10–40}$, (b) $CN_{40–100}$ and (c) $CN_{100–1000}$ on NPF days in

494 Qingdao on February 5-24 simulated from MAC (marked in red), NOCD (marked in

495 blue) and RACD (marked in green) as well as from observations (OBS) (marked in

496 black). All times are local time.

497

498 **3.3 Substantial contributions of SI-SOA to CCN**

499   Compared with the original model setting, after adjusting the growth process of

500   ultrafine particles (RACD), the number concentration of particles tend to decrease,

501   especially for particles above 40 nm. Ultrafine particles above 40 nm are important

502   sources of CCN (Dusek et al., 2006), in this way, the number concentration of CCN

503   also tends to decline. In addition, in the Base case, we found that the model

504   overestimated $CCN_{0.4\%}$ and $CCN_{0.6\%}$, with mean fractional bias being 64% and 87%,

505   respectively. After adjusting the condensation growth process of ultrafine particles,

506   under high supersaturation (i.e., $CCN_{0.4\%}$ and $CCN_{0.6\%}$), the capability of the model in

507   reproducing the CCN is improved. RACD reduces the overestimation of $CCN_{0.4\%}$ and

508    $CCN_{0.6\%}$, with mean fractional bias reduced to 30% and 56%, respectively, although

509   the overestimates still exist (Figs. S5b, c). However, for low supersaturation (i.e.,

510    $CCN_{0.2\%}$), the decrease of number concentration of CCN is too large, and mean

511   fractional bias decreases from 7% to -45% (Fig. S5a), therefore the bias will be

512   further adjusted later.

513   In addition to the growth process, the remaining overestimate of CCN under high

514   SS and underestimate of CCN over low SS is likely to be influenced by the chemical

515   compositions involved in the activation of ultrafine particles into CCN. Specifically,

516   ultrafine particles can grow up to CCN size under certain SS (Pierce and Adams,

517   2007). This process is influenced by both particle size and hygroscopicity, and

518   hygroscopicity is closely related to the chemical composition of particles (Petters and

519   Kreidenweis, 2007). In particular, inorganic compounds generally increase particle

520   hygroscopicity, increasing CCN. SOA has dual effects on CCN since it decreases

521   particle hygroscopicity but also promotes growth of particles, and these two effects

522   are competitive with each other (Wu et al., 2015; Zaveri et al., 2021). Ultrafine

523   particles must grow to a critical size to be activated into CCN (Dusek et al., 2006).

524   SOA act as a major contributor in promoting the condensational growth of ultrafine

525   particles to the critical size, facilitating particles activation into CCN. In contrast,

526   SOA tends to reduce the hygroscopicity of particles, leading to a diminished ability of

527   activation to CCN (Wu et al., 2015). These two competing effects work together and

528   modulate the number of CCN. Moreover, considering that SI-SOA is the main SOA

529   component on ultrafine particles (Fig. S5d), the effect of SI-SOA on CCN is therefore

530   explored in this study.

531   Considering SI-SOA is a product of S/IVOC oxidation, the oxidation rate of

532   S/IVOC is tightly associated with CCN, which likely affects the bias of CCN. In the

533   original model setup, the oxidation rate is set to be a constant of 4×10^{-11} cm^3 $molec^{-1}$

534   s^{-1} for all S/IVOC. However, a recent study (Wu et al., 2021b) proposed that the

535   oxidation rate can be as high as 5×10^{-11} cm^3 $molec^{-1}$ s^{-1} such as for polycyclic

536   aromatic hydrocarbons (PAHs), close to the original model value, but can be as low as

537   half (i.e., 2×10^{-11} cm^3 $molec^{-1}$ s^{-1}) of the original modeling setting for S/IVOC

538   species except PAHs (O-S/IVOCs). It is noteworthy that the oxidation rates of 5×10^{-11}

539   and 2×10^{-11} in general represent the upper and lower bounds (Zhao et al., 2016;

540   Wu et al., 2021b).

541   To delve into how oxidation rates affect CCN, we set up a few numerical

542   experiments (Table 2) to investigate the response of CCN to the oxidation rate of

543   S/IVOC at three supersaturations (0.6%, 0.4%, 0.2%), including cases of High_Yield

544   and Low_Yield. As it is shown in Fig. 4, decreasing the oxidation rate (Low_Yield)

545   leads to a reduction of ~10% of CCN at high supersaturation (i.e., CCN0.6%) as

546   compared to the High_Yield simulation. This behaviour is a consequence of the

547   decrease of particle number concentrations associated with Low_Yield, particular of

548   the particles close to the critical diameter (40–100 nm). In this case, the effect of

549   particle size dominates the hygroscopicity. In contrast, at a lower supersaturation

550   ($CCN_{0.2\%}$), CCN increases by 42% when the oxidation rate is switched from a high to

551   a low value, which is due to the smaller fraction of SI-SOA contributing to particulate

552   mass when the oxidation rate is low. In this case, relative to SOA, a larger fraction of

553   other particle constituents such as inorganics, increase the volume weighted particle

554   hygroscopicity (Dusek et al., 2006) which causes the increase of CCN number. This

555   means that the effect of hygroscopicity on CCN surpasses the influence on particle

556   size at low supersaturations. This conclusion is consistent with the observation

557   conducted by Ma et al. (2016) in the North China Plain in 2013, which suggested that

558   along with the decrease of SS, the particles that can be activated to CCN is more

559   sensitive to changes of particle hygroscopicity.

560
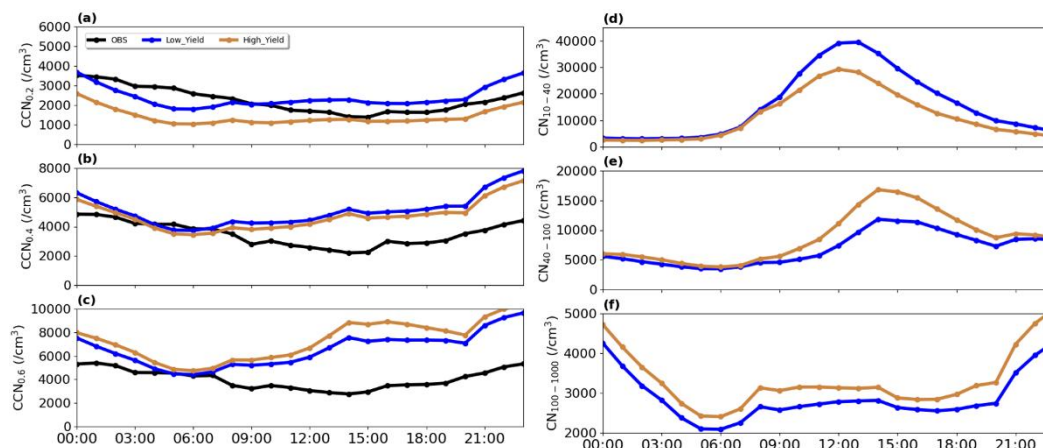
561

562   Fig. 4. Average diurnal variation of (a) $CCN_{0.2\%}$, (b) $CCN_{0.4\%}$ and (c) $CCN_{0.6\%}$ and (d)

563   CN_{10-40}, (e) CN_{40-100}, (f) $CN_{100-1000}$ on NPF days in Qingdao on February 5-24, 2017,

564   in Low_yield and High_yield simulations, shown as blue and brown lines, and black

565   lines represent observation results.

566   Furthermore, compared to the high yield of SI-SOA, the low SI-SOA yield

567   results in a high CCN concentration under low SS and low CCN concentration under

568   high SS. Therefore, both the underestimates of $CCN_{0.2\%}$ (mean fractional bias of -45%)

569   and overestimates of $CCN_{0.6\%}$ (mean fractional bias of 56%) mentioned above are

570   improved, with mean fractional bias of $CCN_{0.2\%}$ and $CCN_{0.6\%}$ reaching 7% and 43%,

571   respectively (Fig. 4a,c). This result suggests that the oxidation rate of S/IVOC is

572   possibly closer to the low value, which is understandable based on Wu et al. (2021b),

573   who found that the amount of O-S/IVOCs, which corresponds to a low oxidation rate,

574   is in general much larger (i.e., 20 times) than that of PAHs with a high oxidation rate.

575   In addition to the single site of Qingdao, we further explore the impact of SI-

576   SOA yield on CCN from a larger spatial coverage (Fig. 5). Consistent with the

577   mechanism revealed over Qingdao, even from a larger spatial perspective, a lower

578   oxidation rate of S/IVOC essentially enhances CCN at a lower SS (e.g., $CCN_{0.2\%}$; Fig.

579   5a) with the highest increase over North China Plain area (Fig. 5a), and weakens CCN

580   (i.e., by 10–20% over Beijing-Tianjin-Hebei) at a higher SS (Fig. 5c), particularly

over the dense emission area (Fig. S12). It is worth noting that in the 2-species VBS mechanism used in our study, all S/IVOC in the inventory is calculated based on a constant emission ratio of S/IVOC to POA from all source categories (Shrivastava et al., 2011), which may miss part of S/IVOC due to different emission ratios of POA from different source (Chang et al., 2022). In addition, the simplified VBS mechanism used in our study does not take into account the multi-step oxidation of organic species, which may introduce some uncertainties. To be more specific, in the 2-species VBS mechanism, SI-SOA with effective saturation concentrations (c^*) of 10^{-2} $\mu g\ m^{-3}$ is formed by the vapor phase oxidation of S/IVOC vapors with c^* of $10^5\ \mu g\ m^{-3}$, reducing volatility by 7 orders of magnitude. The process of one-step oxidation does not mean to represent a physical process, but to parameterize the mean effect of a complex process of SOA formation (Shrivastava et al., 2011). However, in the real atmosphere, the gaseous VOCs often undergo multi-generational oxidation to form SOA (Garmash et al., 2020), during which the properties and composition of SOA change substantially.
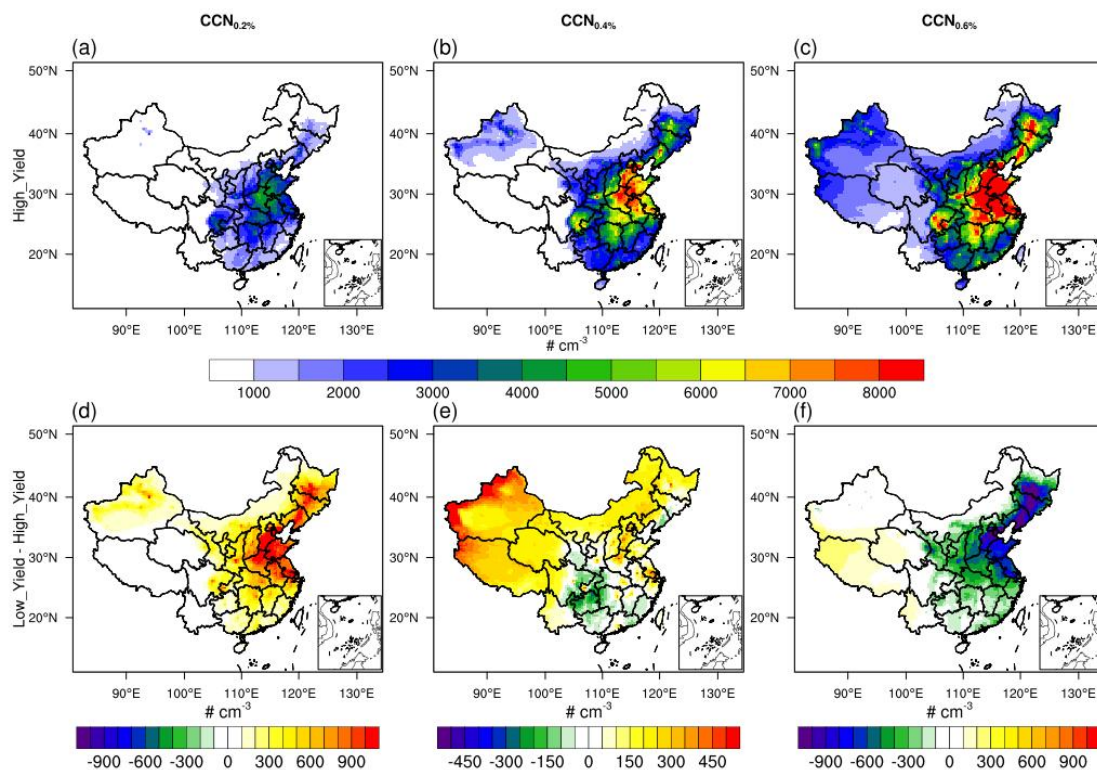
Fig. 5. Spatial distributions of CCN concentrations at different supersaturations (SS), (a) and (d) are $CCN_{0.2\%}$, (b) and (e) are $CCN_{0.4\%}$, and (c) and (f) are $CCN_{0.6\%}$. The top

599 panels exhibit the results from the High_Yield simulation, and the bottom panels

600 shows the difference between the Low_Yield and High_Yield simulations.

601

3.4 Contribution of nucleation to CCN under different SI-SOA yields

603 Considering the importance of nucleated particles on CCN (Yu et al., 2020;

604 Westervelt et al., 2013), we further investigate the influence of nucleation on CCN

605 under different SI-SOA yield conditions discussed above.

606 As shown in Fig. 6, in simulations close to the original model setting

607 (High_Yield), when SS is low (i.e., SS=0.2%), the nucleation process tends to reduce

608 the CCN by ~10–50%. In contrast, when the SS is high (0.6%), the nucleation results

609 in a significant increase in CCN in most regions of China. When the yield of SI-SOA

610 is adjusted to a lower level, the nucleation process has a positive contribution to CCN

611 under both low and high SS. Especially, when SS is low (0.2%), the sign reversal, i.e.,

612 from negative (Fig. 6a) to positive (Fig. 6d) contributions of NPF to CCN along with

613 the decrease of SI-SOA yield, i.e., the increase is concentrated in the eastern China

614 with an average of 10–20%. The primary mechanism lies in that along with the

615 decrease of SI-SOA yield, the smaller fraction of SI-SOA yields an increase in

616 hygroscopicity, which surpasses the suppression effect on particle growth due to

617 reduced SI-SOA formation. In the real atmosphere, when the supersaturation is

618 usually low, e.g. about ~0.1% in polluted areas (Kalkavouras et al., 2019; Hudson and

619 Noble, 2014), CCN will likely reduce with increasing oxidation rate of S/IVOC and

620 corresponding SI-SOA formation.

621
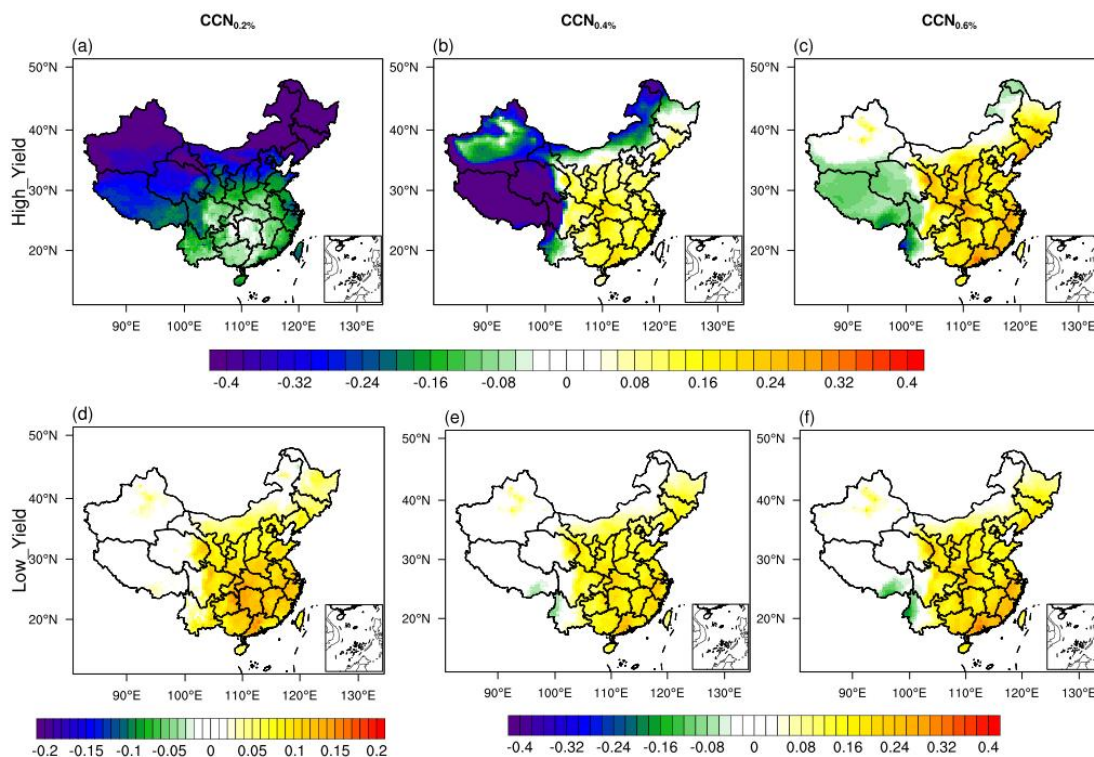
Fig. 6. Spatial distribution of contribution of nucleation to CCN calculated by the ratio of the difference between the parameterization with and without nucleation to the parameterization with nucleation under different SI-SOA yields in China in February 2017. (a), (d) is $CCN_{0.2\%}$,(b), (e) is $CCN_{0.4\%}$,(c), (f) is $CCN_{0.6\%}$.The upper panel and lower panel represent High_Yield and Low_Yield simulation respectively

In addition to the linear-H_2SO_4 nucleation mechanism, one more empirical scheme of kinetics nucleation is selected, which assumes that the nucleation rate is proportional to the square of the concentration of sulfuric acid ($J = K[H_2SO_4]^2$), to investigate the effect of nucleation on CCN. Substantially positive contributions of nucleation to CCN is found when the low SI-SOA yield is applied, consistent with what was shown based on the linear-H_2SO_4 nucleation scheme (Fig. S13). However, nucleation contributes positively to CCN even when the SI-SOA yield is high in the quadratic-H_2SO_4 nucleation scheme (e.g., kinetics nucleation scheme). When more sulfuric acid molecules participate in nucleation under this scheme than the linear-H_2SO_4 nucleation scheme, the particles are more easily hygroscopically activated to CCN, which is equivalent to the effect of a reduction in organic components in the

linear-H_2SO_4 nucleation scheme (e.g., activation-type nucleation scheme). The results from this study show the importance of assessing the simulated effects of the nucleation scheme on not only the formation and growth process of particles but also climate factors such as CCN using observations.

Conclusions

In this study, WRF-Chem explicit-NPF simulations are used to investigate the observed wintertime NPF events and their contribution to CCN in China. Based on observations in a typical coastal city of Qingdao, we identify high biases of the model simulated CN and CCN concentrations. Therefore, we updated and improved the parameterization setting on particle growth in the model, mainly including: (1) adjusting the mass accommodation coefficient (α) to from the default value of 0.1 to 0.65, an important parameter for sulfuric acid condensation; (2) proportionally reducing the condensation amount of nitric acid on particles below 40 nm, (3) changing the emitted low-volatility POA from gas to particle. Through these adjustments, the capability of the model in reproducing CN and CCN is substantially improved, leading to better agreement with the observed results, which significantly reduces the overestimation of CN_{10-40} (mean fractional bias decreases from 48% to 1%) and CN_{40-100} (mean fractional bias decreases from 98% to 63%).

For CCN, due to the crucial role of SI-SOA in promoting the growth of ultrafine particles, on the basis of previous studies, we lower the oxidation rate of S/IVOC and hence the production rate of SI-SOA, which weakens the growth of particles to reach the critical size of CCN activation, but enhances particulate hygroscopicity favoring the activation to CCN. When the yield of SI-SOA is adjusted to the lower bound of literature value, $CCN_{0.6\%}$ is reduced by ~10% and is closer to observations. At low SS ($CCN_{0.2\%}$), the decrease of SI-SOA yield has greater effects on the increase of particle hygroscopicity compared to the effect of the reduction of particle size due to the decrease of condensation growth. It results in an increase of CCN (as large as ~42%) in better agreement with observations. Under low SS conditions, common in the

atmosphere, a 2.5-fold reduction in SI-SOA yield results in a substantial increase of CCN that switches from a negative contribution of new particle formation to CCN from -50%~-10% to a positive contribution of 10~20%. The substantial contribution of new particle formation to CCN under low SS and SI-SOA is applicable to other mechanisms such as kinetics.

Competing interests. At least one of the (co-)authors is a member of the editorial board of Atmospheric Chemistry and Physics.

Acknowledgements. This research was supported by grants from the National Natural Science Foundation of China (42122039) and Fundamental Research Funds for the Central Universities (202072001). Y.W. was supported by the National Science Foundation Atmospheric Chemistry Program. M.S. was supported by the U.S. Department of Energy (DOE) Office of Science, Office of Biological and Environmental Research (BER) through the Early Career Research Program and the Atmospheric System Research (ASR) program.

References:

Arghavani S, Rose C, Banson S, et al. 2022. The Effect of Using a New Parameterization of Nucleation in the WRF-Chem Model on New Particle Formation in a Passive Volcanic Plume. Atmosphere [J], 13(1): 15.

Bergman T, Laaksonen A, Korhonen H, et al. 2015. Geographical and diurnal features of amine-enhanced boundary layer nucleation. Journal of Geophysical Research: Atmospheres [J], 120(18): 9606-9624.

Buchholz R R, Emmons L K, Tilmes.S 2019. The CESM2 Development Team., 2019. CESM2.1/CAM-Chem Instantaneous Output for Boundary Conditions. UCAR/NCAR - Atmospheric Chemistry Observations and Modeling Laboratory.

Bzdek B, Zordan C, Luther G, et al. 2011. Nanoparticle Chemical Composition During New Particle Formation. Aerosol Science and Technology [J], 45(1041-1048.

Bzdek B R, Zordan C A, Pennington M R, et al. 2012. Quantitative Assessment of the Sulfuric Acid Contribution to New Particle Growth. Environmental Science & Technology [J], 46(8): 4365-4373.

Cai C, Zhang X, Wang K, et al. 2016. Incorporation of new particle formation and early growth treatments into WRF/Chem: Model improvement, evaluation, and impacts of anthropogenic aerosols over East Asia. Atmospheric Environment [J], 124(262-284.

Cai J, Chu B, Yao L, et al. 2020. Size-segregated particle number and mass concentrations from different emission sources in urban Beijing. Atmos. Chem. Phys. [J], 20(21): 12721-12740.

Carter W 2000. Documentation of the SAPRC-99 Chemical Mechanism for VOC Reactivity Assessment. Final Report to California Air Resources Board [J].

Chang X, Zhao B, Zheng H, et al. 2022. Full-volatility emission framework corrects missing and underestimated secondary organic aerosol sources. One Earth [J], 5(403-412.

Chang Y, Gao Y, Lu Y, et al. 2021. Discovery of a Potent Source of Gaseous Amines in Urban China. Environmental Science & Technology Letters [J], 8(9): 725-731.

Chen F, Dudhia J 2000. Coupling an Advanced Land-Surface/Hydrology Model with the Penn State/NCAR MM5 Modeling System. 129(

Cheng Y, Su H, Koop T, et al. 2015. Size dependence of phase transitions in aerosol nanoparticles. Nature Communications [J], 6(1): 5923.

Chrit M, Sartelet K, Sciare J, et al. 2018. Modeling organic aerosol concentrations and properties during winter 2014 in the northwestern Mediterranean region. Atmos. Chem. Phys. [J], 18(24): 18079-18100.

Chu B, Kerminen V-M, Bianchi F, et al. 2019. Atmospheric new particle formation in China. Atmospheric Chemistry and Physics [J], 19(115-138.

Dal Maso M, Kulmala M, Riipinen I, et al. 2005. Formation and growth of fresh atmospheric aerosols: Eight years of aerosol size distribution data from SMEAR II, Hyytiälä, Finland. Boreal Environment Research [J], 10(323-336.

Davidovits P, Worsnop D R, Jayne J T, et al. 2004. Mass accommodation coefficient of water vapor on liquid water. Geophysical Research Letters [J], 31(22).

Donahue N M, Robinson A L, Stanier C O, et al. 2006. Coupled Partitioning, Dilution, and Chemical Aging of Semivolatile Organics. Environmental Science & Technology [J], 40(8): 2635-2643.

Dong C, Matsui H, Spak S, et al. 2019. Impacts of New Particle Formation on Short-term Meteorology and Air Quality as Determined by the NPF-explicit WRF-Chem in the Midwestern United States. Aerosol and Air Quality Research [J], 19(2): 204-220.

Dusek U, Frank G P, Hildebrandt L, et al. 2006. Size Matters More Than Chemistry for Cloud-Nucleating Ability of Aerosol Particles. Science [J], 312(5778): 1375-1378.

Ehn M, Thornton J, Kleist E, et al. 2014. A large source of low-volatility secondary organic aerosol. Nature [J], 506(476-479.

Fanourgakis G S, Kanakidou M, Nenes A, et al. 2019. Evaluation of global simulations of aerosol particle and cloud condensation nuclei number, with implications for cloud droplet formation. Atmos. Chem. Phys. [J], 19(13): 8591-8617.

Gordon H, Kirkby J, Baltensperger U, et al. 2017. Causes and importance of new particle formation in the present-day and preindustrial atmospheres. 122(16): 8739-8760.

Grell G A 1993. Prognostic Evaluation of Assumptions Used by Cumulus Parameterizations. Monthly Weather Review [J], 121(3): 764-787.

Guo S, Hu M, Zamora M L, et al. 2014. Elucidating severe urban haze formation in China. Proceedings of the National Academy of Sciences [J], 111(49): 17373-17378.

Hong S-Y, Noh Y, Dudhia J 2006. A New Vertical Diffusion Package with an Explicit Treatment of Entrainment Processes. Monthly Weather Review - MON WEATHER REV [J], 134(

Hudson J G, Noble S 2014. CCN and Vertical Velocity Influences on Droplet Concentrations and Supersaturations in Clean and Polluted Stratus Clouds. Journal of the Atmospheric Sciences [J], 71(1): 312-331.

Iacono M, Delamere J, Mlawer E, et al. 2008. Radiative Forcing by Long-Lived Greenhouse Gases: Calculations with the AER Radiative Transfer Models. Journal of Geophysical Research [J], 113(

Jimenez J L, Canagaratna M R, Donahue N M, et al. 2009. Evolution of Organic Aerosols in the Atmosphere. Science [J], 326(5959): 1525-1529.

Kalkavouras P, Bougiatioti A, Kalivitis N, et al. 2019. Regional new particle formation as modulators of cloud condensation nuclei and cloud droplet number in the eastern Mediterranean. Atmos. Chem. Phys. [J], 19(9): 6185-6203.

Kerminen V-M, Chen X, Vakkari V, et al. 2018. Atmospheric new particle formation and growth: Review of field observations. Environmental Research Letters [J], 13(

Krechmer J E, Day D A, Ziemann P J, et al. 2017. Direct Measurements of Gas/Particle Partitioning and Mass Accommodation Coefficients in Environmental Chambers. Environ Sci Technol [J], 51(20): 11867-11875.

Kulmala M, Dada L, Daellenbach K R, et al. 2021. Is reducing new particle formation a plausible solution to mitigate particulate air pollution in Beijing and other Chinese megacities? Faraday Discussions [J], 226(0): 334-347.

Kulmala M, L L, Lehtinen K, et al. 2004. Initial steps of aerosol growth. Atmospheric Chemistry and Physics [J], 4(

Kulmala M, Petäjä T, Ehn M, et al. 2013. Chemistry of Atmospheric Nucleation: On the Recent Advances on Precursor Characterization and Atmospheric Cluster Composition in Connection with Atmospheric New Particle Formation. Annual review of physical chemistry [J], 65(

Kulmala M, Petäjä T, Nieminen T, et al. 2012. Measurement of the nucleation of atmospheric aerosol particles. Nature Protocols [J], 7(9): 1651-1667.

Lai S, Hai S, Gao Y, et al. 2022. The striking effect of vertical mixing in the planetary boundary layer on new particle formation in the Yangtze River Delta. Science of The Total Environment [J], 829(154607.

Lee S-H, Gordon H, Yu H, et al. 2019. New Particle Formation in the Atmosphere: From Molecular Clusters to Global Climate. Journal of Geophysical Research: Atmospheres [J], 124(

Li K, Zhu Y, Gao H, et al. 2015. A comparative study of cloud condensation nuclei measured between non-heating and heating periods at a suburb site of Qingdao in the North China. Atmospheric Environment [J], 112(40-53.

Li M, Liu H, Geng G, et al. 2017. Anthropogenic emission inventories in China: a review. National Science Review [J], 4(6): 834-866.

Li X, Li Y, Cai R, et al. 2022. Insufficient Condensable Organic Vapors Lead to Slow Growth of New Particles in an Urban Environment. Environmental Science & Technology [J], 56(14): 9936-9946.

Liu H J, Zhao C S, Nekat B, et al. 2014a. Aerosol hygroscopicity derived from size-segregated chemical composition and its parameterization in the North China Plain. Atmos. Chem. Phys. [J], 14(5): 2525-2539.

Liu M, Matsui H 2022. Secondary Organic Aerosol Formation Regulates Cloud Condensation Nuclei in the Global Remote Troposphere. Geophysical Research Letters [J], 49(18): e2022GL100543.

Liu X, Zhu Y, Zheng M, et al. 2014b. Production and growth of new particles during two cruise campaigns in the marginal seas of China. Atmospheric Chemistry and Physics [J], 14(

793   Liu X H, Zhu Y J, Zheng M, et al. 2014c. Production and growth of new particles during two cruise
794   campaigns in the marginal seas of China. Atmos. Chem. Phys. [J], 14(15): 7941-7951.

795   Lovejoy E R, Curtius J, Froyd K D 2004. Atmospheric ion-induced nucleation of sulfuric acid and
796   water. Journal of Geophysical Research: Atmospheres [J], 109(D8).

797   Lu H, Wang G, Guo H 2022. Ambient acidic ultrafine particles in different land-use areas in two
798   representative Chinese cities. Science of The Total Environment [J], 830(154774.

799   Lu Y, Yan C, Fu Y, et al. 2019. A proxy for atmospheric daytime gaseous sulfuric acid concentration in
800   urban Beijing. Atmos. Chem. Phys. [J], 19(3): 1971-1983.

801   Lupascu A, Easter R, Zaveri R, et al. 2015. Modeling particle nucleation and growth over northern
802   California during the 2010 CARES campaign. Atmos. Chem. Phys. [J], 15(21): 12283-12313.

803   Ma N, Zhao C, Tao J, et al. 2016. Variation of CCN activity during new particle formation events in the
804   North China Plain. Atmos. Chem. Phys. [J], 16(13): 8593-8607.

805   Matsui H, Koike M, Kondo Y, et al. 2011. Impact of new particle formation on the concentrations of
806   aerosols and cloud condensation nuclei around Beijing. Journal of Geophysical Research:
807   Atmospheres [J], 116(D19).

808   Matsui H, Koike M, Takegawa N, et al. 2013. Spatial and temporal variations of new particle formation
809   in East Asia using an NPF-explicit WRF-chem model: North-south contrast in new particle
810   formation frequency. 118(20): 11,647-611,663.

811   Merikanto J, Spracklen D V, Mann G W, et al. 2009. Impact of nucleation on global CCN. Atmos.
812   Chem. Phys. [J], 9(21): 8601-8616.

813   Mikkonen S, Romakkaniemi S, Smith J N, et al. 2011. A statistical proxy for sulphuric acid
814   concentration. Atmos. Chem. Phys. [J], 11(21): 11319-11334.

815   Morrison H, Thompson G, Tatarskii V 2009. Impact of Cloud Microphysics on the Development of
816   Trailing Stratiform Precipitation in a Simulated Squall Line: Comparison of One and Two-
817   Moment Schemes. Monthly Weather Review - MON WEATHER REV [J], 137(991-1007.

818   Napari I, Noppel M, Vehkamäki H, et al. 2002. Parametrization of ternary nucleation rates for H2SO4-
819   NH3-H2O vapors. Journal of Geophysical Research: Atmospheres [J], 107(D19): AAC 6-1-
820   AAC 6-6.

821   Nieminen T, Kerminen V M, Petäjä T, et al. 2018. Global analysis of continental boundary layer new
822   particle formation based on long-term measurements. Atmos. Chem. Phys. [J], 18(19): 14737-
823   14756.

824   Petäjä T, Mauldin I R L, Kosciuch E, et al. 2009. Sulfuric acid and OH concentrations in a boreal forest
825   site. Atmos. Chem. Phys. [J], 9(19): 7435-7448.

826   Pierce J, Riipinen I, Kulmala M, et al. 2011. Quantification of the volatility of secondary organic
827   compounds in ultrafine particles during nucleation events. Atmospheric Chemistry and
828   Physics Discussions [J], 11(14495-14539.

829   Pöschl U, Canagaratna M, Jayne J T, et al. 1998. Mass Accommodation Coefficient of H2SO4 Vapor
830   on Aqueous Sulfuric Acid Surfaces and Gaseous Diffusion Coefficient of H2SO4 in N2/H2O.
831   The Journal of Physical Chemistry A [J], 102(49): 10082-10089.

832   Qiao X, Yan C, Li X, et al. 2021. Contribution of Atmospheric Oxygenated Organic Compounds to
833   Particle Growth in an Urban Environment. Environmental Science & Technology [J], XXXX(

834   Ren J, Chen L, Fan T, et al. 2021. The NPF Effect on CCN Number Concentrations: A Review and Re-
835   Evaluation of Observations From 35 Sites Worldwide. Geophysical Research Letters [J],
836   48(19): e2021GL095190.

837   Riipinen I, Sihto S L, Kulmala M, et al. 2007. Connections between atmospheric sulphuric acid and
838   new particle formation during QUEST III–IV campaigns in Heidelberg and Hyytiälä.
839   Atmos. Chem. Phys. [J], 7(8): 1899-1914.

840   Roldin P, Swietlicki E, Massling A, et al. 2011a. Aerosol ageing in an urban plume – implication for
841   climate. Atmos. Chem. Phys. [J], 11(12): 5897-5915.

842   Roldin P, Swietlicki E, Schurgers G, et al. 2011b. Development and evaluation of the aerosol dynamics
843   and gas phase chemistry model ADCHEM. Atmos. Chem. Phys. [J], 11(12): 5867-5896.

844   Saha S, Moorthi S, Wu X, et al. 2014. The NCEP Climate Forecast System Version 2. Journal of
845   Climate [J], 27(6): 2185-2208.

846   Shen X, Sun J, Zhang X, et al. 2018. Comparison of Submicron Particles at a Rural and an Urban Site
847   in the North China Plain during the December 2016 Heavy Pollution Episodes. Journal of
848   Meteorological Research [J], 32(26-37.

849   Shrivastava M, Fast J, Easter R, et al. 2011. Modeling organic aerosols in a megacity: comparison of
850   simple and complex representations of the volatility basis set approach. Atmospheric
851   Chemistry and Physics [J], 11(6639-6662.

852   Shrivastava M K, Lane T E, Donahue N M, et al. 2008. Effects of gas particle partitioning and aging of
853   primary emissions on urban and regional organic aerosol concentrations. 113(D18).

854   Sihto S L, Kulmala M, Kerminen V M, et al. 2006. Atmospheric sulphuric acid and aerosol formation:
855   implications from atmospheric measurements for nucleation and early growth mechanisms.
856   Atmos. Chem. Phys. [J], 6(12): 4079-4091.

857   Sihto S L, Mikkilä J, Vanhanen J, et al. 2011. Seasonal variation of CCN concentrations and aerosol
858   activation properties in boreal forest. Atmos. Chem. Phys. [J], 11(24): 13269-13285.

859   Tewari M, Wang W, Dudhia J, et al. 2016. Implementation and verification of the united NOAH land
860   surface model in the WRF model [M].

861   Virtanen A, Kannosto J, Kuuluvainen H, et al. 2011. Bounce behavior of freshly nucleated biogenic
862   secondary organic aerosol particles. Atmos. Chem. Phys. [J], 11(16): 8759-8766.

863   Wang D-W, Guo H, Chan C K 2014. Diffusion Sampler for Measurement of Acidic Ultrafine Particles
864   in the Atmosphere. Aerosol Science and Technology [J], 48(12): 1236-1246.

865   Wang J, Li M, Li L, et al. 2022. Particle number size distribution and new particle formation in Xiamen,
866   the coastal city of Southeast China in wintertime. Science of The Total Environment [J],
867   826(154208.

868   Westervelt D M, Pierce J R, Riipinen I, et al. 2013. Formation and growth of nucleated particles into
869   cloud condensation nuclei: model–measurement comparison. Atmos. Chem. Phys. [J], 13(15):
870   7645-7663.

871   Wu H, Li Z, Jiang M, et al. 2021a. Contributions of traffic emissions and new particle formation to the
872   ultrafine particle size distribution in the megacity of Beijing. Atmospheric Environment [J],
873   262(118652.

874   Wu L, Ling Z, Shao M, et al. 2021b. Roles of Semivolatile/Intermediate-Volatility Organic Compounds
875   on SOA Formation Over China During a Pollution Episode: Sensitivity Analysis and
876   Implications for Future Studies. Journal of Geophysical Research: Atmospheres [J], 126(8):
877   e2020JD033999.

878   Wu Z, Hu M, Yue D, et al. 2011. Evolution of particle number size distribution in an urban atmosphere
879   during episodes of heavy pollution and new particle formation. Science China Earth Sciences
880   [J], 54(11): 1772.

881 Yao L, Garmash O, Bianchi F, et al. 2018. Atmospheric new particle formation from sulfuric acid and
882   amines in a Chinese megacity. Science [J], 361(278-281.

883 Yu F 2005. Quasi-unary homogeneous nucleation of H2SO4-H2O. The Journal of Chemical Physics [J],
884   122(7): 074501.

885 Yu F, Luo G, Nair A A, et al. 2020. Wintertime new particle formation and its contribution to cloud
886   condensation nuclei in the Northeastern United States. Atmos. Chem. Phys. [J], 20(4): 2591-
887   2601.

888 Yu F, Luo G, Pryor S C, et al. 2015. Spring and summer contrast in new particle formation over nine
889   forest areas in North America. Atmos. Chem. Phys. [J], 15(24): 13993-14003.

890 Yuan Q, Li W, Zhou S, et al. 2015. Integrated evaluation of aerosols during haze-fog episodes at one
891   regional background site in North China Plain. Atmospheric Research [J], 156(102-110.

892 Yue D L, Hu M, Zhang R Y, et al. 2011. Potential contribution of new particle formation to cloud
893   condensation nuclei in Beijing. Atmospheric Environment [J], 45(33): 6070-6077.

894 Zaveri R A, Easter R C, Fast J D, et al. 2008. Model for Simulating Aerosol Interactions and Chemistry
895   (MOSAIC). 113(D13).

896 Zaveri R A, Easter R C, Peters L K 2005. A computationally efficient Multicomponent Equilibrium
897   Solver for Aerosols (MESA). Journal of Geophysical Research: Atmospheres [J], 110(D24).

898 Zhang Q, Jimenez J L, Canagaratna M R, et al. 2007. Ubiquity and dominance of oxygenated species
899   in organic aerosols in anthropogenically-influenced Northern Hemisphere midlatitudes.
900   Geophysical Research Letters [J], 34(13).

901 Zhao B, Wang S, Donahue N M, et al. 2016. Quantifying the effect of organic aerosol aging and
902   intermediate-volatility emissions on regional-scale aerosol pollution in China. Scientific
903   Reports [J], 6(1): 28815.

904 Zheng B, Tong D, Li M, et al. 2018. Trends in China's anthropogenic emissions since 2010 as the
905   consequence of clean air actions. Atmos. Chem. Phys. [J], 18(19): 14095-14111.

906 Zhu Y, Li K, Shen Y, et al. 2019. New particle formation in the marine atmosphere during seven cruise
907   campaigns. Atmos. Chem. Phys. [J], 19(1): 89-113.

908 Zhu Y, Sabaliauskas K, Liu X, et al. 2014. Comparative analysis of new particle formation events in
909   less and severely polluted urban atmosphere. Atmospheric Environment [J], 98(655-664.

910 Zhu Y, Shen Y, Li K, et al. 2021. Investigation of Particle Number Concentrations and New Particle
911   Formation With Largely Reduced Air Pollutant Emissions at a Coastal Semi-Urban Site in
912   Northern China. Journal of Geophysical Research: Atmospheres [J], 126(17): e2021JD035419.

913

914